ACS Catalysis

pubs.acs.org/acscatalysis

Research Article

Single Metal Atom Catalysts and ORR: H-Bonding, Solvation, and the Elusive Hydroperoxyl Intermediate

Francesco Armillotta, Davide Bidoggia, Stefania Baronio, Pietro Biasin, Antonio Annese, Mattia Scardamaglia, Suyun Zhu, Benedetto Bozzini, Silvio Modesti, Maria Peressi, and Erik Vesselli*

Cite This: *ACS Catal.* 2022, 12, 7950–7959

Read Online

ACCESS | Metrics & More | Article Recommendations | Supporting Information

ABSTRACT: The widely investigated oxygen reduction reaction (ORR) is well-known to proceed via two competing routes, involving two or four electrons, and yielding different reaction products, respectively. Both pathways are believed to share a common, elusive intermediate, namely, the hydroperoxyl radical. By exploiting a cobalt single-atom biomimetic model catalyst, based on a self-assembled monolayer of Co-porphyrins grown on an almost free-standing graphene sheet, we identify, in situ at room temperature in O2+H2O atmosphere, a hydroperoxyl-water cluster that is stabilized at the Co single-metal atom catalytic site. We show that the interplay between charge transfer, dipole and H-bonding, and water solvation behavior actually determines the hydroperoxyl-water complex stability, the Co-OOH bonding geometry, and, prospectively, opens to the engineered control of the selectivity of ORR pathways.

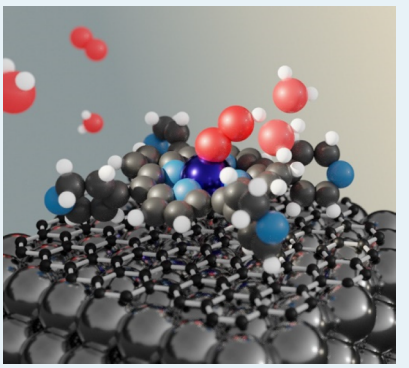

KEYWORDS: *single-atom catalysts, solvation, hydroperoxyl, oxygen reduction reaction, energy transfer, SFG*

1. INTRODUCTION

The O_2 reduction reaction (ORR) can follow two different and competing pathways: direct reduction to OH groups via the $4e^-$ mechanism ($O_2 + 2H_2O + 4e^- \rightarrow 4OH^-$)), or indirect reduction through hydrogen peroxide ($O_2 + H_2O + 2e^- \rightarrow HO_2^- + OH^-$; $HO_2^- + H_2O + 2e^- \rightarrow 3OH^-$; $2HO_2^- \rightarrow O_2 + 2OH^-$) according to the $2e^-$ pathway.[1] ORR is of paramount importance in biology as well as in (photo-)(electro-)catalysis. In the latter case, the process, together with its oxidative counterpart, that is, the oxygen evolution reaction (OER), is becoming increasingly strategic in several technological contexts. These include the perspective of designing efficient bifunctional electrodes for a novel generation of metal-air secondary batteries,[2,3] in particular with Zn anodes and aqueous electrolytes, either of the traditional alkaline type[4] or innovative neutral ones,[5,6] as well as recently proposed solid-state ionic conductors.[7] These devices are highly prospective for tomorrow's green energy scenarios and enable the bypass of many issues associated with state-of-the-art Li-ion based technologies, chiefly the following: volumetric energy density,[8] sustainability,[9] environmental friendliness,[10] recyclability,[11] safety,[12] and durability.[13] Vast literature is already available, carefully investigating, dissecting, and reviewing the ORR mechanism in different environments and phases, and on several catalytic materials (metals, oxides, metallorganic synthetic materials, heme proteins, enzymes....). Since its first observation,[14] the hydroperoxyl molecule (O_2H) has gained the widely accepted role of the fundamental reaction intermediate, being involved in the very initial steps of the reaction of O_2 with water.[15] The O_2H radical actually steers the process along a preferential path between the competing $4e^-$ and $2e^-$ alternative routes, yielding dramatic differences in the reaction kinetics and final products.[6] It represents the key to a thorough, deep insight into the details of the ORR mechanism and its control. Many theoretical/computational papers describe the stability of this molecule, its bonding geometry to catalytically active metal sites, and the energetics of the fundamental ORR reaction steps.[16−18] The influence of solvation is tackled in detail at the fundamental level but only in the gas phase, shedding light onto the stability and properties of H_2O-O_2H clusters[19−22] and the reactivity of singlet dioxygen species.[23] Despite all these efforts, the O_2H intermediate has shown an elusive behavior up to now, and thus, both its stability and its effective, actual role in steering the ORR reaction pathway are liable to be questioned. Pioneering *in situ* spectroscopic evidence of the formation of O_2H and its role in the ORR was obtained very recently on model single-crystal Pt terminations, leaving however an open point about the possible role of "solution species".[24,25] Indeed, while the adsorbed reaction intermediates were successfully

Received: April 25, 2022
Revised: June 7, 2022
Published: June 20, 2022

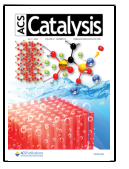

characterized, the second interaction sphere with the solvent could not be experimentally addressed.

We show here how the formation of hydroperoxyl is associated with its stabilization by a surprising combination of charge transfer, dipole, and chemical H-bonding with physisorbed water. We work at room temperature and exploit a single-atom catalyst (SAC) at near-ambient pressure (NAP) conditions within the framework of a biomimetic approach. From a surface catalysis point of view, the latter is generally based on macrocycles containing transition metals, or on 2D materials with metal−nitrogen-carbon bonds, showing very promising results,[26,26−30] obtained by mimicking at surfaces many typical features of enzymatic active sites,[31] including trans-effects,[32−34] local coordination environment, and secondary porphyrin structure.[35] Specifically, atomic-site electrocatalysts may allow selectivity tuning toward the $2e^-$ or $4e^-$ pathway. In fact, this is essentially determined by the O−O heterolytic scission barrier in any of the reaction intermediates[36] and, ultimately, by the geometric and electronic configuration of the hydroperoxyl species,[15,37] whose formation follows a Pauling-type O_2 preadsorption and activation to a superoxide species (O_2^-) at the catalytic sites.[17,34,38,39] Recent fundamental advances have allowed the investigation of biomimetic tetrapyrrole-based 2D materials beyond UHV surface science conditions, up to the solid−gas and solid−liquid interfaces.[33,34,38,40−43] Here, we report the spectroscopic evidence obtained at room temperature of a stable O_2H-H_2O/Co complex at the solid−gas interface, at the limit of water condensation conditions. The system is characterized *in situ* at NAP by combining infrared-visible sum-frequency generation (IR-Vis SFG), pump−probe IR-Vis SFG, and ambient-pressure high-energy-resolution synchrotron radiation X-ray photoelectron (AP-XPS) spectroscopies. Complementary information is obtained in ultrahigh vacuum (UHV) by means of scanning tunneling microscopy (STM), IR-Vis SFG, and XPS, while fundamental insight is obtained by means of *ab initio* calculations performed within the framework of density functional theory (DFT).

2. EXPERIMENTAL AND THEORETICAL METHODS

2.1. Sample Preparation. The Ir(111) surface was cleaned by standard cycles of Ar^+ sputtering and annealing @1300−1350 K, alternated with treatments in oxygen background in the 330−1070 K temperature range. Before growing graphene, the sample was finally annealed to 1300−1350 K in UHV. Graphene was grown by thermal cracking of ethylene dosed from the background *in vacuo*, following established recipes.[44] In detail, after saturation with ethylene at room temperature, the crystal was annealed to 1100 K. At 1100 K, an ethylene background was introduced, and the temperature was further increased up to 1300 K. A temperature cycle (1300−500−1300 K) followed, always in ethylene background. The complete GR growth treatment lasted about 40 min. The quality of graphene was checked by monitoring the corresponding LEED pattern. 5,10,15,20-tetra(4-pyridyl)-21*H*,23*H*-porphyrin Co(III) chloride (CoTPyP) porphyrins were purchased from Frontier Scientific. The molecular source was a heated boron nitride crucible (570 K). The deposition flux (0.15 ML/min at the sample surface) was monitored by means of a quartz microbalance. Long outgassing of the molecules in UHV was necessary to get rid of the residual organic contaminants. The CoTPyP deposition on graphene/Ir(111) was performed with the sample kept at 500 K in a residual background pressure of 5×10^{-10} mbar. The chloride ligand in the CoTPyP detaches from the molecule in the evaporation process.[45,46] Cobalt was chosen in this pilot study because of its known good activity in the form of single-atom catalyst with respect to the ORR.[45]

2.2. IR-Vis Sum Frequency Generation. IR-Vis sum frequency generation vibronic spectroscopy is a nonlinear optical technique.[47,48] The measurements were performed in a dedicated setup at the Department of Physics of the University of Trieste.[49] A UHV system with a base pressure of 5×10^{-11} mbar hosting standard surface science preparation and characterization techniques is directly coupled with a high-pressure cell for *in situ* IR-Vis SFG spectroscopy. The reactor is equipped with a gas system to handle the reactants' pressure in the 10^{-9}−10^{+2} mbar range. The inlet and outlet of the laser beams are provided by UHV- compatible BaF_2 windows. The Ir(111) disc was mounted on Ta wires, also used for resistive heating. The excitation source (Ekspla, 1064 nm, 30 ps, 50 Hz) delivers a 532 nm (2.33 eV) second harmonic visible beam and IR radiation, tunable in the 1000−4500 cm^{-1} range, obtained thanks to harmonic and parametric generation. The raw spectra are normalized to the impinging IR and Vis excitation intensities and then to a reference spectrum of clean Al or GaAs to take into account the roto-vibrational absorption features due to H_2O and CO_2, depending on the energy range, along the optical path of the IR beam in air before entering the cell. The normalized SFG spectra were then analyzed by least-squares fitting to a parametric, effective expression of the nonlinear second-order susceptibility.[47,50,51] The expression 1 well reproduces the observed lineshapes, accounting for the resonant IR-Vis vibronic transitions and the nonresonant background and describing all the interference terms:

$$\frac{I_{SFG}(\omega_{IR})}{I_{VIS}I_{IR}(\omega_{IR})} \propto \left| A_{NRes} + \sum \frac{A_k e^{i\Delta\varphi_k}}{k\omega_{IR} - \omega_k + i\Gamma_k} \right|^2 \quad (1)$$

A_{NRes} and A_k account for the amplitudes of the nonresonant and k^{th}-resonant contributions, respectively. $\Delta\varphi_k$ is the phase difference between the k^{th}-resonant and nonresonant signals. ω_k is the energy position of the line and Γ_k its Lorentzian broadening, related to the dephasing rate, which in turn stems from the energy lifetime and the elastic dephasing of the excited vibronic state.[52] In the main text, we plot the normalized IR−Vis SFG signal intensity (dots), together with the best fit (lines) and the deconvolution of each resonance with its interference with the nonresonant background (color-filled profiles). The latter are calculated with the parameters obtained from the fitting procedure following:

$$\frac{I_{SFG,k}(\omega_{IR})}{I_{VIS}I_{IR}(\omega_{IR})} \propto \left| A_{NRes} + \frac{A_k e^{i\Delta\varphi_k}}{\omega_{IR} - \omega_k + i\Gamma_k} \right|^2 \quad (2)$$

These plots interestingly put in direct evidence the amplitude and the relative phase for each of the resonances. Further details and examples can be found in our previous work.[42,43,50] In the present study, all spectra were collected in the ppp polarization configuration (SFG-visible-infrared), unless otherwise specified.

2.3. Ambient Pressure X-ray Photoelectron Spectroscopy. Near-ambient pressure X-ray photoelectron spectroscopy (AP-XPS) experiments were performed at the HIPPIE beamline of the MAX IV synchrotron radiation facility in Lund (S), allowing *in situ* and *operando* measurements in gaseous

https://doi.org/10.1021/acscatal.2c02029
ACS Catal. 2022, 12, 7950−7959

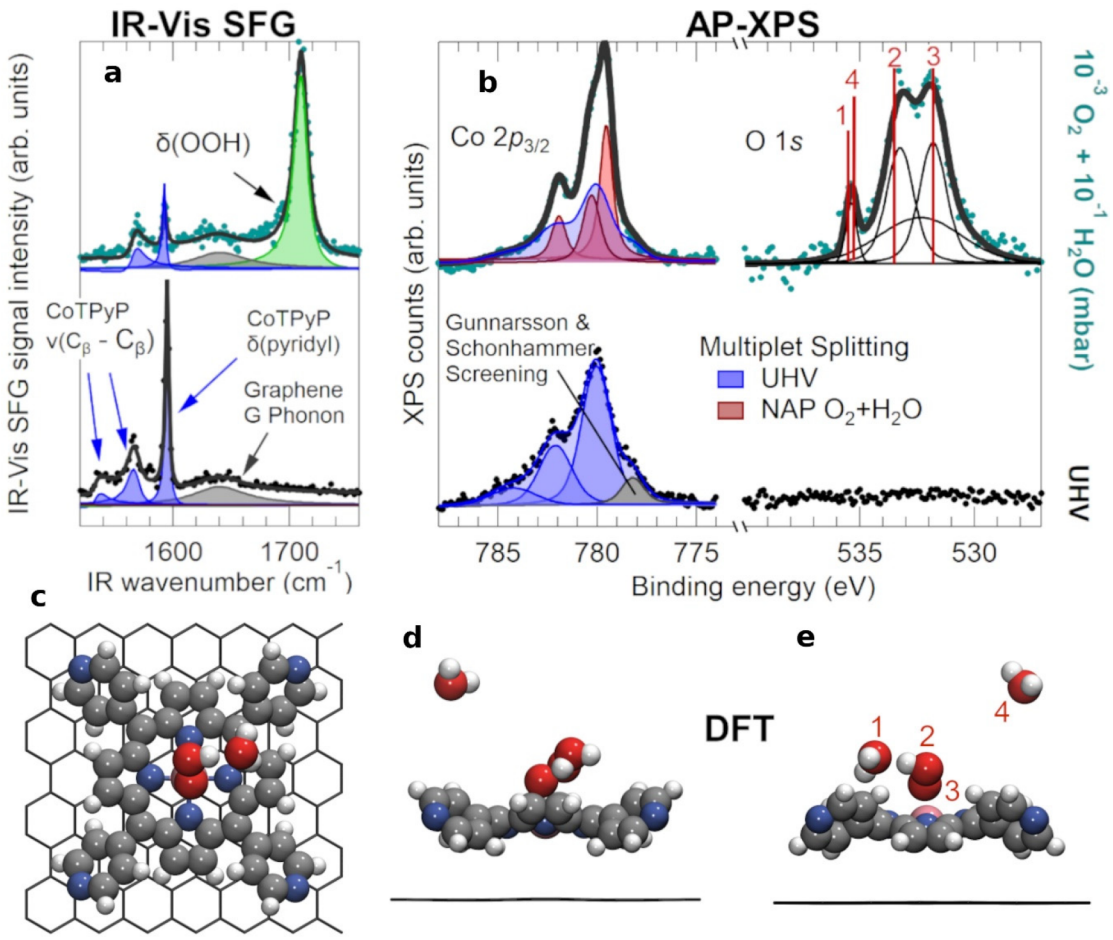

Figure 1. Spectroscopic and geometric characterization of the hydroperoxyl-water complex. (a) IR-Vis SFG spectra of the pristine CoTPyP/GR layer in UHV (bottom) and in 10^{-3} mbar O_2 + 10^{-1} mbar H_2O at room temperature (top); experimental data (markers) are reported together with the best fit (continuous lines) and deconvolution envelopes (filled profiles).[50] (b) NAP-XPS spectra of the Co $2p_{3/2}$ (left, $h\nu$ = 910 eV) and O 1s (right, $h\nu$ = 660 eV) core levels corresponding to the same conditions as in (A); red vertical lines indicate the binding energies obtained for the optimized O_2H-H_2O complex on CoTPyP/GR from *ab initio* DFT calculations for different O 1s core levels, as labeled in (e): 1 − physisorbed/wetting water, 2 − OOH, 3 − OOH, 4 − gas phase water. (c) Top view of the DFT optimized model of the O_2H-H_2O/Co/TPyP/GR system. (d,e) Side views of the same system with an additional water molecule in the gas phase from two different points of view, to show the order-2 rotational symmetry of the CoTPyP, with a saddle shape macrocycle and peripheral pyridyl groups alternatively rotated by +39° and −39° with respect to GR.

atmosphere.[53] C, N, and O 1s, and Co 2p3/2 core levels were measured to check sample preparation and contamination in UHV, as well as in the *in situ* experiments. Photon energies of 400, 514, 660, and 910 eV were chosen, respectively, in order to optimize photoionization cross section, surface sensitivity, and, thus, the signal-to-noise ratio. The CoTPyP/GR/Ir(111) system was exposed to O_2 (5×10^{-3} mbar), H_2O (5×10^{-2} mbar), and O_2+H_2O ($5 \times 10^{-3} + 5 \times 10^{-2}$ mbar, respectively) at room temperature. The binding energy scale was calibrated with respect to the Ir $4f_{7/2}$ core level (60.87 eV) as a reference.[54] The NAP-XPS Spectra were best fitted by least-squares fitting methods according to the Doniach-Šunjić or Voigt lineshapes,[55] depending on the core level, after subtraction of a linear background.

2.4. Density Functional Theory Calculations. *Model Systems.* We described the CoTPyP molecule on GR using a periodically repeated simulation supercell with 6 × 8 GR unit cells, with negligible interactions with adjacent images. This choice was justified by the focus of the present work, which is the interaction between the O_2H-H_2O complex and the CoTPyP molecule rather than a precise description of the molecular layer. Because of the small interaction between GR and the Ir(111) substrate, the latter was neglected in order to minimize the computational effort. However, the CoTPyP−GR interaction could not be ignored, yielding an adsorption energy of 1.95 eV/molecule and determining the CoTPyP geometric and electronic structures.

Technicalities. All DFT calculations were performed using the open source Quantum ESPRESSO package,[56−58] based on plane waves and pseudopotentials approach. The exchange correlation energy was described by the Perdew−Burke−Ernzerhof (PBE) functional within the generalized gradient approximation (GGA) method. Vanderbilt ultrasoft pseudopotentials were employed except for the Co atom, for which a Rappe−Rabe−Kaxiras−Joannopoulos ultrasoft pseudopotential was used, instead.[59] For an efficient treatment of the Co 3d states we used the Hubbard-U correction[60] with an U parameter of 3.5 eV in order to recover the 5.5 eV distance between occupied and unoccupied $3d_{z2}$ levels, as suggested in the literature.[61] van der Waals interactions were included through the Grimme DFT-D3 approach.[62] A plane-wave basis set with energy cutoff of 60 Ry was used for the wave

https://doi.org/10.1021/acscatal.2c02029
ACS Catal. 2022, 12, 7950−7959

functions, together with a 240 Ry cutoff for the charge density. Because of the metallic behavior of the system, a Methfessel−Paxton scheme[63] was used for the occupation of the electronic states, with a smearing of 0.01 Ry. Brillouin zone integration was performed with a Monkhorst−Pack 4 × 4 × 4 k-point sampling grid for self-consistent field (SCF) calculations and on a 8 × 8 × 8 grid for NSCF (nonself-consistent field) calculations. Optimized structures were obtained using the Broyden, Fletcher, Goldfarb, and Shanno algorithm with energy and force convergence threshold of 1.0×10^{-6} Ry and 1.0×10^{-3} a.u. respectively. After full optimization of the CoTPyP/GR system, which leads to an almost flat GR layer, the optimization of the structures with adsorbed O_2H and, subsequently, H_2O, was made keeping GR fixed. Oxygen core level shifts were obtained from total energy differences between SCF calculations, in which one O atom at a time was described by a pseudopotential taking into account a full core hole in 1s state, using the final state approximation.[64] In order to investigate the bonding nature of the O_2H-H_2O/Co system, we used different postprocessing tools. All the plots showing electron density rearrangement due to adsorption of component B on component A were calculated as the difference in electron density distribution between the full system (A+B) and the individual, separated components in the positions assumed in the total system:

$$\Delta n(\mathbf{r}) - n_{A+B}(\mathbf{r}) - (n_A + n_B)(\mathbf{r})$$

In order to identify the character and the strength of the interaction, the reduced density gradient (RDG) ($s(\mathbf{r}) = \frac{1}{2(3\pi^2)^{1/3}} \frac{|\nabla n(\mathbf{r})|}{n^{4/3}}$) was calculated together with the electron density multiplied by the sign of the second Hessian eigenvalue, following.[65] Indeed, while low values of $s(\mathbf{r})$ identify noncovalent bonding regions at constant electron density, the second Hessian eigenvalue λ_2 is known to distinguish between regions of bonding ($\lambda_2 < 0$) and steric repulsion ($\lambda_2 > 0$). Along with its sign, the magnitude of the interaction is estimated from the values of the density itself; therefore, we use $sgn(\lambda_2)n(\mathbf{r})$ as a color scale in RDG plots. Spatially resolved energy-integrated local density of states (ILDOS) was calculated in order to visualize charge density in bonding regions. Interesting energy regions to calculate ILDOS were identified by comparing the projected density of states (PDOS) of a bonding configuration with respect to the PDOS of the individual, separated constituents. Oxidation states for the Co metal center were determined according to the literature,[66] counting the number of valence electrons to be assigned to the atom as the number of its fully occupied 3d-orbitals (i.e., Löwding population of the orbital = 1).

3. RESULTS AND DISCUSSION

O_2 and H_2O are dosed at room temperature on an ordered monolayer of cobalt tetrapyridyl-porphyrins (CoTPyP) deposited and self-assembled on an almost free-standing graphene (GR) single sheet of excellent crystalline quality (grown *in situ* on the Ir(111) single crystal termination[67] and checked with LEED). The pristine CoTPyP monolayer displays an almost rhombic unit cell, yielding a super-Moiré coincidence pattern with the underlying GR/Ir(111) support (Figure S1). The local geometry of the self-assembled layer is more distorted with respect to the almost square cell previously observed for similar porphyrins and phthalocyanines on GR/Ir(111)[43,68] and on Au(111).[69−71] The corresponding IR-Vis SFG spectrum is characterized in the 1500−1750 cm^{-1} range by the presence of four main vibronic resonances (Figure 1a, bottom panel; Table S1), ascribed to the ν_{C-C} modes at 1535 and 1567 cm^{-1} and to the δ_{pyr} mode at 1595 cm^{-1} of the porphyrins,[72−74] together with the GR/Ir(111) G phonon that shifts from 1608 to 1639 cm^{-1} after the CoTPyP deposition.[42,43] Exposure of the 2D system at room temperature to $p_{O_2} = 10^{-3}$ mbar or to $p_{H_2O} = 10^{-1}$ mbar yields neither substantial vibrational (IR-Vis SFG), nor electronic (AP-XPS) spectroscopic modifications with respect to the pristine layer (Figures S1−S2). The graphene sheet is known to be unreactive under these mild conditions, completely passivating the underlying Ir termination.[42] Instead, exposure of the surface to the mixture of the two gases (Figure 1a, top panel) yields dramatic changes, with rates depending on the order in which the reactants are introduced (Figure S2). While only slight energy shifts and phase changes of the resonances associated with the CoTPyP/GR layer are detected, the growth of a new, very intense resonance at 1710 cm^{-1} is observed both in ppp and ssp polarization combinations (Figure S3a). The feature can be attributed to the δ_{OOH} mode of O_2H in a metastable O_2H-H_2O complex, in remarkable agreement with previous predictive calculations about the dynamical behavior of hydroperoxyl radical water clusters, including the enhanced spectroscopic cross section.[20,21] We find that the complex reacts/dissolves already after mild heating (Figure S3b) above room temperature, coherently with an enhancement of the surface reaction rate toward a mass-transport-limited condition. Exposure of the CoTPyP monolayer to the oxygen/water mixture is also associated with the growth of O 1*s* core level components (Figure 1b, right) in the AP-XPS spectra. We can distinguish the contribution from water at 535.4 eV[75] plus two features at 533.4 and 531.8 eV, respectively. *Ab initio* DFT calculations of the O_2H-H_2O/CoTPyP/GR system (Figure 1c−e) yield an optimized structure in which a water molecule participates in the formation of a stable complex with the hydroperoxyl radical. The computed O 1s core level binding energies for the different O species (from 1 to 4) are in remarkable agreement with the spectroscopic line positions (vertical, red lines in Figure 1b, right), thus allowing their straightforward interpretation and confirming the vibrational assignment. Specifically, we attribute the peak at 535.4 eV to both gas phase (4) and physisorbed/wetting (1) water. The peaks at 533.4 (531.8) eV are assigned to the O**O**H (**O**OH) ligand at the Co site (numbers 2 and 3, respectively, in Figure 1e). Accordingly, the two latter peaks are observed to grow in parallel and with almost equal intensity as a function of the background gases pressure. A broad, almost Gaussian contribution progressively develops at 532.4 eV upon aging (hours of exposure) of the sample, associated with OH, OH-OH, O-H_2O, C-O poisoning at defective sites, and GR oxidation,[75−77] indicating its slow degradation. The Co $2p_{3/2}$ core level line shape is strongly influenced by the reaction (Figure 1b, left), displaying a strong remodulation of the multiplet splitting structure with respect to the pristine sample, showing an intensity decrease of the components at 784.3, 782.1, and 780.1 eV and the growth of new peaks at 781.9, 780.3, and 779.6 eV. In a very recent report on Co-based metalorganic frameworks,[78] the latter component was associated with CoOOH species. The lowest binding energy feature that is evident at 778.2 eV on the "as grown" sample is due to the Gunnarsson and Schonhammer transfer of the

https://doi.org/10.1021/acscatal.2c02029
ACS Catal. 2022, 12, 7950−7959

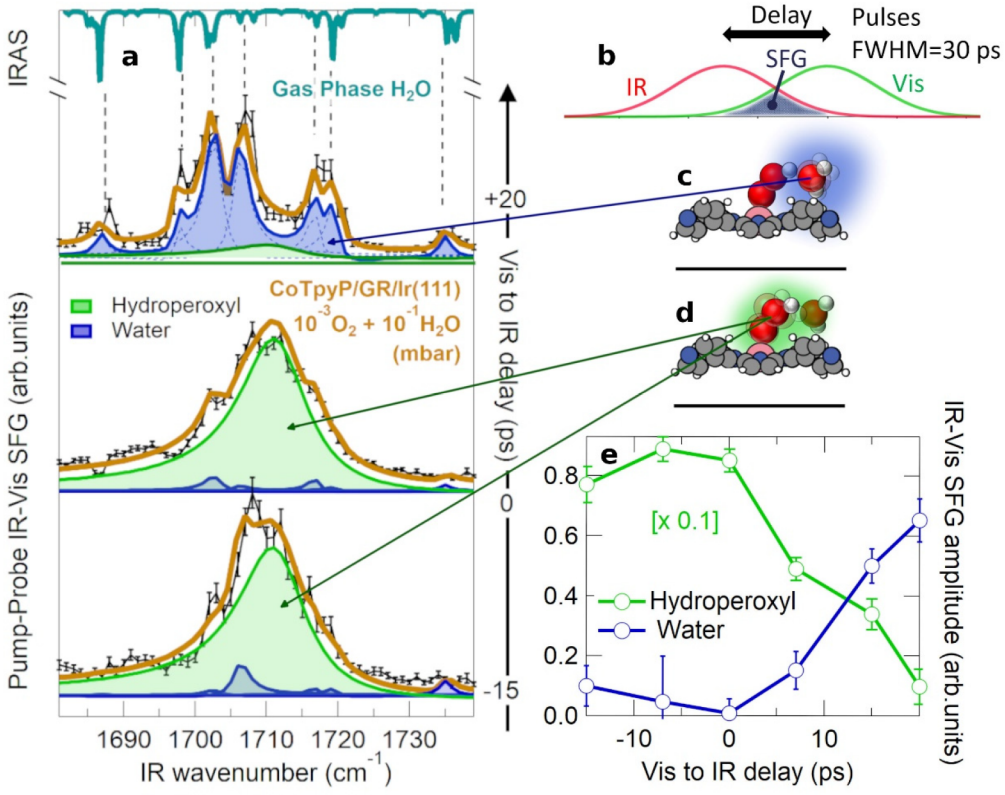

Figure 2. Energy coupling and stabilization of the ligated hydroperoxyl-water cluster. (a) IR-Vis SFG spectra of the evolution of the δ_{OOH} mode line shape at 1710 cm^{-1} as a function of the Vis-to-IR delay; the spectra were normalized by the overlap integral of the IR and Vis pulses and are reported together with the best fit (continuous lines) and deconvolution envelopes (filled profiles);[50] in the top part, IR roto-vibrational spectrum of gas phase water simulated with SpectraPlot.[83] (b) Sketch of the delayed IR and Vis pulsed used to generate the time-resolved SF signal. (c,d) Best structural model of the O_2H-H_2O/CoTPyP/GR system as obtained from DFT calculations (as in Figure 1c−e), evidencing the contribution of the different moieties to the spectral evolution reported in (a) and (b); GR is only sketched for better clarity. (e) Normalized IR-Vis SFG amplitude of the OOH and water modes obtained from the fit as a function of the IR-to-Vis delay (see SI for further details).

screening charge.[79,80] The observed quenching of the latter peak upon exposure to the water/oxygen mixture witnesses binding of the ligands to the Co metal site,[81] possibly associated with a change of the metal oxidation state.[77,82] From the O 1s and Co $2p_{3/2}$ core level intensities reported in Figure 1b the complex surface coverage can be estimated. Specifically, in the case of the adopted experimental conditions, the majority of the single-atom Co sites host the water and hydroperoxyl ligands. Because of the size of the porphyrins, however, this yields a surface coverage of only a few percent of a monolayer with respect to the underlying metal termination, representing an exceptional experimental challenge in terms of sensitivity and signal-to-noise ratio. To investigate the role of the O_2H−H_2O interaction, we implemented a pump−probe IR-Vis SFG approach, measuring the SFG response as a function of the IR-to-Vis pulse delay (Figure 2a−d). When the system is pre-excited with the IR pulse, we observe that the vibronic energy of the δ_{OOH} resonance is transferred to the water roto-vibrational modes[83] on a 10 ps time-scale (Figure 2e, Figure S4). This indicates strong coupling between the hydroperoxyl species and coadsorbed water. The latter phenomenon is known to participate in the stabilization of the complex, in analogy to what is theoretically predicted[19−23,84] and observed by 2D-IR spectroscopy, regarding hydration shell reorganization and H-bonding exchange.[85] Similarly, the hydrogen bond strengthening, followed by relaxation and thermalization, mediating the energy transfer process, was observed in liquid water.[86] While it was found that the former process occurs on a 0.1−1 ps time scale, vibrational energy is then efficiently funneled through the H-bonding network into all degrees of freedom in water on a several-ps time scale, in agreement with our observations. This leads to an increased local temperature, as water vibrations are known to have strongly mixed intra- and intermolecular character.[86,87] Similar mechanisms take place also in heme enzymatic reaction centers. In Hb/Mb, an imidazole group of the protein histidine residue provides a stabilizing H-bonded network for the Fe-peroxo intermediate[88] so that, by artificially engineering the H-bonding structure of Mb, the protein can be modified to promote O_2 reduction to water via the $4e^-$ mechanism.[89] In synthesized Fe porphyrin complexes, the H bonding network is exploited to promote protonation to specifically form the hydroperoxide intermediate complex.[90,91] In the case of the system discussed here, we find that water directly participates in the stable O_2H-H_2O complex with concurrent bonding and energy transfer mechanisms, while O_2H binds directly to the Co center. The picture is consolidated by our *ab initio* simulations, yielding a high complex-CoTPyP binding energy of 6.12 eV for the more stable configuration with the terminal $O^{(3)}$ atom of hydroperoxyl bound to the metal center (Co-OOH, Figure 3a, bottom panel), in line with calculations on a similar model system.[18] Most interestingly, upon bonding, three phenomena take place in parallel, contributing to the stabilization of the whole system: (i) 0.15 e^- are transferred

https://doi.org/10.1021/acscatal.2c02029
ACS Catal. 2022, 12, 7950−7959

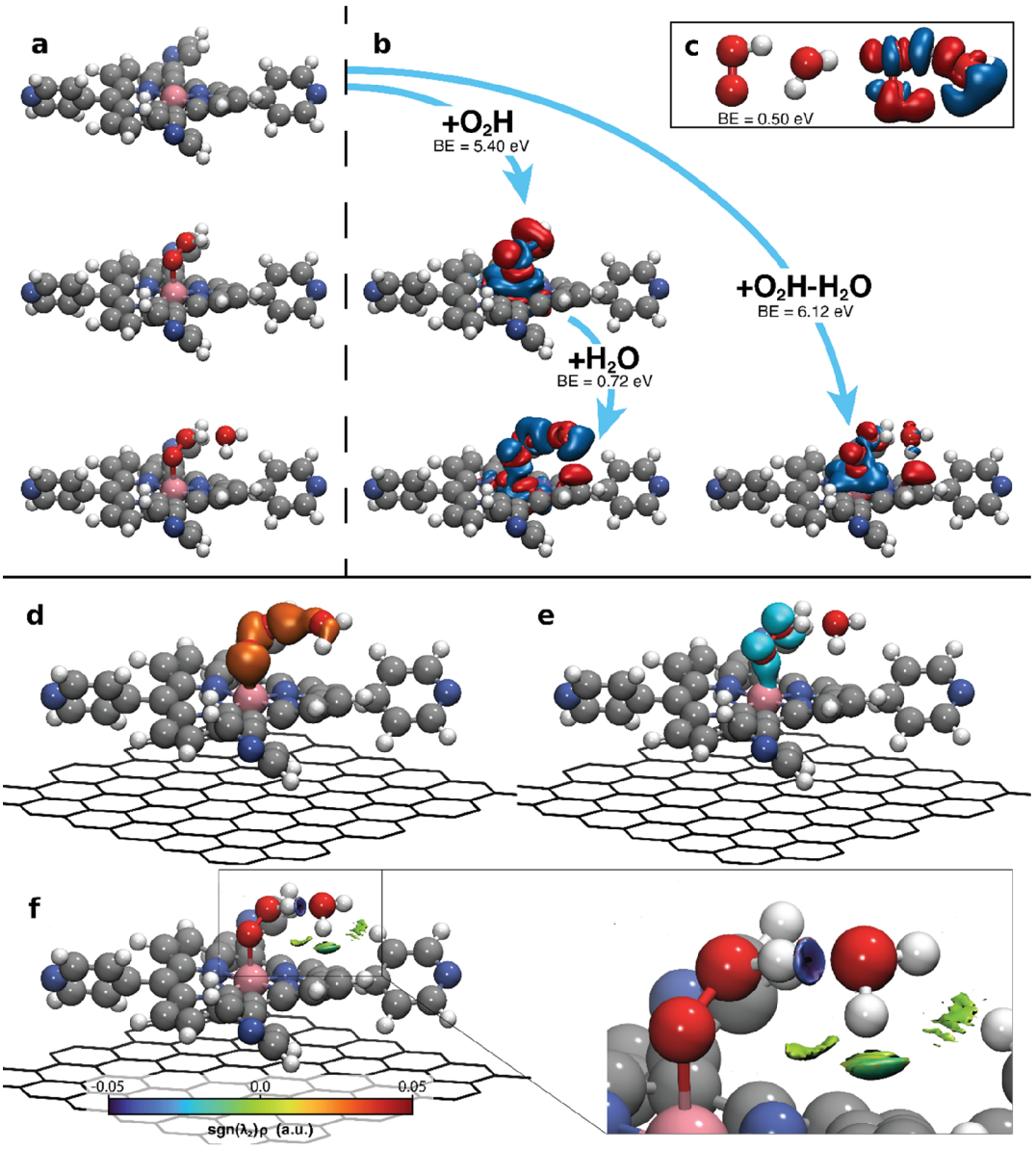

Figure 3. *Ab initio* insight on the bonding nature of the O_2H-H_2O/Co system. (a) From top to bottom, optimized models for CoTPyP/GR, O_2H/CoTPyP/GR, O_2H-H_2O/CoTPyP/GR, showing that CoTPyP is globally unaffected by the adsorption of O_2H and H_2O, apart from a small lifting of the Co atom by 0.16 Å. (b) Bonding-induced rearrangement of the electron density distribution in the O_2H-H_2O/CoTPyP/GR system, with respect to the individual constituents. Isosurfaces upon adsorption of: (left) first O_2H and then H_2O; (right) the whole O_2H-H_2O complex (red/blue for electron gain/loss, isovalues: ±0.001 au). (c) Optimized configuration of the complex in gas phase, and electron charge redistribution upon complex formation—isosurfaces as in (B). (d, e) Spatially resolved Local Density of States integrated in two relevant energy ranges (Figure S6) (surfaces isovalue: 0.005 au). In (D) the charge accumulation in the O_2H−H_2O bonding region is visible, and in both (D) and (E) the hybridization of the Co $3d_{z2}$ and 2p orbitals of the terminal O atom of O_2H ($O^{(3)}$ in Figure 1E). (f) Visualization of noncovalent interactions by means of an isosurface of the Reduced Energy Gradient (RDG): the blue color of the isosurface between O_2H and H_2O indicates a region with rather strong noncovalent bonding, and the green color of the isosurface between H_2O and the pyrrolic and pyridinic moieties of the CoTPyP indicates a region with moderate noncovalent bonding (RDG value: 0.6 au, with color depending of the local value of the electron density; see Supporting Information for details).

from the CoTPyP inner macrocycle to both O atoms of O_2H (Figure S5) through the Co $3d_{z2}$ atomic orbital hybridization with the ligand's orbitals (Figure 3d,e); (ii) O_2H and H_2O form a strong hydrogen-mediated bond within the complex, with charge accumulation in the bond (Figure 3d,f); (iii) long-range van der Waals forces, associated with charge redistribution and dipole formation, develop extensively among the water molecule, hydroperoxyl, and adjacent pyrrolic and pyridinic moieties of the CoTPyP (Figure 3f). Interestingly, also hydroperoxyl alone would be strongly bonded to the Co metal center (by 5.40 eV) (Figure 3a,b, central panels), inducing a change of oxidation state in the Co atom, from +2 of the pristine CoTPyP on graphene to +3. However, water addition induces a charge redistribution also in the Co-OOH bond (Figure 3b, bottom left panel), restoring the oxidation state of the Co atom to a + 2 value. The simultaneous adsorption of O_2H and H_2O on the Co atom, with the water molecule interacting also with adjacent moieties of the tetrapyrrole, stabilizes the complex itself, whose binding energy increases by 0.22 eV with respect to the gas-phase

https://doi.org/10.1021/acscatal.2c02029
ACS Catal. 2022, 12, 7950−7959

configuration (Figure 3c). A second adsorption geometry for hydroperoxyl, in which binding to Co occurs via the central $O^{(2)}$ atom (Co-OHO), is less favorable by only 160 meV, implying that both configurations (Co-OOH and Co-OHO) could be populated in principle, depending on the temperature and on the local surrounding environment.

4. CONCLUSIONS

By means of a combination of *in situ* measurements and theoretical methods, we have shown that a cobalt single-atom biomimetic model catalyst, based on a self-assembled monolayer of Co-porphyrins grown on an almost free-standing graphene sheet, stabilizes a hydroperoxyl-water cluster at room temperature in O_2+H_2O atmosphere. The interplay between charge transfer, dipole and H-bonding, and water solvation is found to determine ultimately the stability and bonding geometries, unveiling the core step of the ORR. This teases the mind toward a picture in which selectivity for $2e^-$ vs $4e^-$ ORR could be driven by the configuration of the hydroperoxyl ligand at the catalysts' active site, ultimately defined by the unraveled interplay between charge transfer, chemical, dipole, and H-bonding (solvation) phenomena,[22] thus paving the way toward novel approaches to the reaction control.

■ ASSOCIATED CONTENT

Supporting Information

The Supporting Information is available free of charge at https://pubs.acs.org/doi/10.1021/acscatal.2c02029.

Additional STM, XPS, and SFG experimental data, additional time-resolved and temperature-dependent information; corroborating theoretical results; best-fitting parameters of spectroscopic data; additional references (PDF)

■ AUTHOR INFORMATION

Corresponding Author

Erik Vesselli − *Department of Physics, University of Trieste, 34127 Trieste, Italy; CNR-IOM, 34149 Basovizza, Trieste, Italy; Center for Energy, Environment and Transport Giacomo Ciamician, University of Trieste, 34127 Trieste, Italy;* orcid.org/0000-0002-6799-0032; Email: evesselli@units.it

Authors

Francesco Armillotta − *Department of Physics, University of Trieste, 34127 Trieste, Italy*

Davide Bidoggia − *Department of Physics, University of Trieste, 34127 Trieste, Italy*

Stefania Baronio − *Department of Physics, University of Trieste, 34127 Trieste, Italy*

Pietro Biasin − *Department of Physics, University of Trieste, 34127 Trieste, Italy*

Antonio Annese − *Department of Physics, University of Trieste, 34127 Trieste, Italy*

Mattia Scardamaglia − *MAX IV Laboratory, 224 84 Lund, Sweden;* orcid.org/0000-0002-1128-7524

Suyun Zhu − *MAX IV Laboratory, 224 84 Lund, Sweden*

Benedetto Bozzini − *Department of Energy, Politecnico di Milano, 20156 Milano, Italy*

Silvio Modesti − *Department of Physics, University of Trieste, 34127 Trieste, Italy; CNR-IOM, 34149 Basovizza, Trieste, Italy*

Maria Peressi − *Department of Physics, University of Trieste, 34127 Trieste, Italy;* orcid.org/0000-0001-6142-776X

Complete contact information is available at: https://pubs.acs.org/10.1021/acscatal.2c02029

Author Contributions

The research project was conceptualized by E.V. The experiments were mainly carried out by F.A., D.B., S.B., P.B., M.S., S.Z., and S.M. Funding was obtained by M.P, and E.V. The project was administrated and supervised by M.P and E.V. The draft was originally written by F.A., D.B., and E.V. All coauthors contributed equally.

Notes

The authors declare no competing financial interest.

■ ACKNOWLEDGMENTS

We acknowledge MAX IV Laboratory for time on Beamline HIPPIE under Proposal 20190694. Research conducted at MAX IV, a Swedish national user facility, is supported by the Swedish Research council under contract 2018-07152, the Swedish Governmental Agency for Innovation Systems under contract 2018-04969, and Formas under contract 2019-02496 We acknowledge access to the Cineca high performance computers, funding from Italian MUR (grant PRIN 2017KFY7XF) and Università degli Studi di Trieste (grant FRA2021).

■ REFERENCES

(1) Bozzini, B.; Altissimo, M.; Amati, M.; Bocchetta, P.; Gianoncelli, A.; Gregoratti, L.; Kourousias, G.; Mancini, L.; Mele, C.; Kiskinova, M. In Situ and Ex Situ X-Ray Microspectroelectrochemical Methods for the Study of Zinc−Air Batteries. In *Encyclopedia of Interfacial Chemistry*; Wandelt, K., Ed.; Elsevier, 2018; pp 174−194.

(2) Liu, Q.; Pan, Z.; Wang, E.; An, L.; Sun, G. Aqueous Metal-Air Batteries: Fundamentals and Applications. *Energy Storage Mater.* **2020**, *27*, 478−505.

(3) Li, T.; Peng, X.; Cui, P.; Shi, G.; Yang, W.; Chen, Z.; Huang, Y.; Chen, Y.; Peng, J.; Zou, R.; Zeng, X.; Yu, J.; Gan, J.; Mu, Z.; Chen, Y.; Zeng, J.; Liu, J.; Yang, Y.; Wei, Y.; et al. Recent Progress and Future Perspectives of Flexible Metal-air Batteries. *SmartMat* **2021**, *2*, 519−553.

(4) Leong, K. W.; Wang, Y.; Ni, M.; Pan, W.; Luo, S.; Leung, D. Y. C. Rechargeable Zn-Air Batteries: Recent Trends and Future Perspectives. *Renew. Sustain. Energy Rev.* **2022**, *154*, 111771.

(5) Wang, C.; Li, J.; Zhou, Z.; Pan, Y.; Yu, Z.; Pei, Z.; Zhao, S.; Wei, L.; Chen, Y. Rechargeable Zinc-Air Batteries with Neutral Electrolytes: Recent Advances, Challenges, and Prospects. *EnergyChem.* **2021**, *3*, 100055.

(6) Sun, W.; Wang, F.; Zhang, B.; Zhang, M.; KüPers, V.; Ji, X.; Theile, C.; Bieker, P.; Xu, K.; Wang, C.; Winter, M. A Rechargeable Zinc-Air Battery Based on Zinc Peroxide Chemistry. *Science* **2021**, *371*, 46−51.

(7) Zuo, Y.; Wang, K.; Zhao, S.; Wei, M.; Liu, X.; Zhang, P.; Xiao, Y.; Xiong, J. A High Areal Capacity Solid-State Zinc-Air Battery via Interface Optimization of Electrode and Electrolyte. *Chem. Eng. J.* **2022**, *430*, 132996.

(8) Son, Y.; Cha, H.; Jo, C.; Groombridge, A. S.; Lee, T.; Boies, A.; Cho, J.; De Volder, M. Reliable Protocols for Calculating the Specific Energy and Energy Density of Li-Ion Batteries. *Mater. Today Energy* **2021**, *21*, 100838.

(9) Yu, X.; Manthiram, A. Sustainable Battery Materials for Next-Generation Electrical Energy Storage. *Adv. Energy Sustain. Res.* **2021**, *2*, 2000102.

(10) Clark, S.; Bleken, F. L.; Stier, S.; Flores, E.; Andersen, C. W.; Marcinek, M.; Szczesna-Chrzan, A.; Gaberscek, M.; Palacin, M. R.;

Uhrin, M.; Friis, J. Toward a Unified Description of Battery Data. *Adv. Energy Mater.* **2021**, *12*, 2102702.
(11) Miao, Y.; Liu, L.; Zhang, Y.; Tan, Q.; Li, J. An Overview of Global Power Lithium-Ion Batteries and Associated Critical Metal Recycling. *J. Hazard. Mater.* **2022**, *425*, 127900.
(12) Wang, H.; Liu, B.; Xu, C.; Jin, C.; Li, K.; Du, Z.; Wang, Q.; Ouyang, M.; Feng, X. Dynamic Thermophysical Modeling of Thermal Runaway Propagation and Parametric Sensitivity Analysis for Large Format Lithium-Ion Battery Modules. *J. Power Sources* **2022**, *520*, 230724.
(13) Hu, X.; Xu, L.; Lin, X.; Pecht, M. Battery Lifetime Prognostics. *Joule* **2020**, *4*, 310−346.
(14) Foner, S. N.; Hudson, R. L. Detection of the HO2 Radical by Mass Spectrometry. *J. Chem. Phys.* **1953**, *21*, 1608−1609.
(15) Zhao, D.; Zhuang, Z.; Cao, X.; Zhang, C.; Peng, Q.; Chen, C.; Li, Y. Atomic Site Electrocatalysts for Water Splitting, Oxygen Reduction and Selective Oxidation. *Chem. Soc. Rev.* **2020**, *49*, 2215−2264.
(16) Gao, J.; Yang, H. b.; Huang, X.; Hung, S.-F.; Cai, W.; Jia, C.; Miao, S.; Chen, H. M.; Yang, X.; Huang, Y.; Zhang, T.; Liu, B. Enabling Direct H2O2 Production in Acidic Media through Rational Design of Transition Metal Single Atom Catalyst. *Chem.* **2020**, *6*, 658−674.
(17) Gao, J.; Liu, B. Progress of Electrochemical Hydrogen Peroxide Synthesis over Single Atom Catalysts. *ACS Mater. Lett.* **2020**, *2*, 1008−1024.
(18) Xiao, Y.; Zhang, W. High-Throughput Calculation Investigations on the Electrocatalytic Activity of Codoped Single Metal−Nitrogen Embedded in Graphene for ORR Mechanism. *Electrocatalysis* **2020**, *11*, 393−404.
(19) Suma, K.; Sumiyoshi, Y.; Endo, Y. The Rotational Spectrum of the Water-Hydroperoxy Radical (H2O-HO2) Complex. *Science* **2006**, *311*, 1278−1281.
(20) Aloisio, S.; Francisco, J. S. Existence of a Hydroperoxy and Water (HO2 ·H2O) Radical Complex. *J. Phys. Chem. A* **1998**, *102*, 1899−1902.
(21) Iyengar, S. S. Dynamical Effects on Vibrational and Electronic Spectra of Hydroperoxyl Radical Water Clusters. *J. Chem. Phys.* **2005**, *123*, 084310.
(22) Hernández-Soto, H.; Weinhold, F.; Francisco, J. S. Radical Hydrogen Bonding: Origin of Stability of Radical-Molecule Complexes. *J. Chem. Phys.* **2007**, *127*, 164102.
(23) Xu, X.; Muller, R. P.; Goddard, W. A. The Gas Phase Reaction of Singlet Dioxygen with Water: A Water-Catalyzed Mechanism. *Proc. Natl. Acad. Sci.* **2002**, *99*, 3376−3381.
(24) Dong, J.-C.; Zhang, X.-G.; Briega-Martos, V.; Jin, X.; Yang, J.; Chen, S.; Yang, Z.-L.; Wu, D.-Y.; Feliu, J. M.; Williams, C. T.; Tian, Z.-Q.; Li, J.-F. In Situ Raman Spectroscopic Evidence for Oxygen Reduction Reaction Intermediates at Platinum Single-Crystal Surfaces. *Nat. Energy* **2019**, *4*, 60−67.
(25) Dong, J.-C.; Su, M.; Briega-Martos, V.; Li, L.; Le, J.-B.; Radjenovic, P.; Zhou, X.-S.; Feliu, J. M.; Tian, Z.-Q.; Li, J.-F. Direct In Situ Raman Spectroscopic Evidence of Oxygen Reduction Reaction Intermediates at High-Index Pt(Hkl) Surfaces. *J. Am. Chem. Soc.* **2020**, *142*, 715−719.
(26) Bozzini, B.; Kourousias, G.; Bedolla, D. E.; Gianoncelli, A. Chemical-State Evolution of Ni in Mn Ni/Polypyrrole Nanocomposites under Bifunctional Air Electrode Conditions, Investigated by Quasi-in Situ Multi-Scale Soft X-Ray Absorption Spectroscopy. *Mater. Today Energy* **2017**, *6*, 154−163.
(27) Bocchetta, P.; Amati, M.; Gregoratti, L.; Kiskinova, M.; Sezen, H.; Taurino, A.; Bozzini, B. Morphochemical Evolution during Ageing of Pyrolysed Mn/Polypyrrole Nanocomposite Oxygen Reduction Electrocatalysts: A Study Based on Quasi-in Situ Photoelectron Spectromicroscopy. *J. Electroanal. Chem.* **2015**, *758*, 191−200.
(28) Bozzini, B.; Bocchetta, P.; Alemán, B.; Amati, M.; Gianoncelli, A.; Gregoratti, L.; Sezen, H.; Taurino, A.; Kiskinova, M. Electrodeposition and Pyrolysis of Mn/Polypyrrole Nanocomposites: A Study Based on Soft X-Ray Absorption, Fluorescence and Photoelectron Microspectroscopies. *J. Mater. Chem. A* **2015**, *3*, 19155−19167.
(29) Bocchetta, P.; Alemán, B.; Amati, M.; Fanetti, M.; Goldoni, A.; Gregoratti, L.; Kiskinova, M.; Mele, C.; Sezen, H.; Bozzini, B. ORR Stability of Mn−Co/Polypyrrole Nanocomposite Electrocatalysts Studied by Quasi in-Situ Identical-Location Photoelectron Microspectroscopy. *Electrochem. commun* **2016**, *69*, 50−54.
(30) Tylus, U.; Jia, Q.; Strickland, K.; Ramaswamy, N.; Serov, A.; Atanassov, P.; Mukerjee, S. Elucidating Oxygen Reduction Active Sites in Pyrolyzed Metal−Nitrogen Coordinated Non-Precious-Metal Electrocatalyst Systems. *J. Phys. Chem. C* **2014**, *118*, 8999−9008.
(31) Gutzler, R.; Stepanow, S.; Grumelli, D.; Lingenfelder, M.; Kern, K. Mimicking Enzymatic Active Sites on Surfaces for Energy Conversion Chemistry. *Acc. Chem. Res.* **2015**, *48*, 2132−2139.
(32) Hieringer, W.; Flechtner, K.; Kretschmann, A.; Seufert, K.; Auwärter, W.; Barth, J. V.; Görling, A.; Steinrück, H.-P.; Gottfried, J. M. The Surface Trans Effect: Influence of Axial Ligands on the Surface Chemical Bonds of Adsorbed Metalloporphyrins. *J. Am. Chem. Soc.* **2011**, *133*, 6206−6222.
(33) Vesselli, E. Tetrapyrroles at Near-Ambient Pressure: Porphyrins and Phthalocyanines beyond the Pressure Gap. *J. Phys. Mater.* **2020**, *3*, 022002.
(34) Vesselli, E. Stabilization and Activation of Molecular Oxygen at Biomimetic Tetrapyrroles on Surfaces: From UHV to near-Ambient Pressure. *Nanoscale Adv.* **2021**, *3*, 1319−1330.
(35) Brezny, A. C.; Nedzbala, H. S.; Mayer, J. M. Multiple Selectivity-Determining Mechanisms of H 2 O 2 Formation in Iron Porphyrin-Catalysed Oxygen Reduction. *Chem. Commun.* **2021**, *57*, 1202−1205.
(36) Huang, X.; Groves, J. T. Oxygen Activation and Radical Transformations in Heme Proteins and Metalloporphyrins. *Chem. Rev.* **2018**, *118*, 2491−2553.
(37) Hooley, R. J. Taking on the Turnover Challenge. *Nat. Chem.* **2016**, *8*, 202−204.
(38) Armillotta, F.; Pividori, A.; Stredansky, M.; Seriani, N.; Vesselli, E. Dioxygen at Biomimetic Single Metal-Atom Sites: Stabilization or Activation? The Case of CoTPyP/Au(111). *Top. Catal* **2020**, *63*, 1585−1595.
(39) Bozzini, B.; Previdi, A.; Amati, M.; Bevilacqua, M.; Cordaro, G.; Corva, M.; Donazzi, A.; Dotelli, G.; Gregoratti, L.; Pelosato, R.; Vorokhta, M.; Vesselli, E. In Situ Near-Ambient Pressure X-Ray Photoelectron Spectroscopy Discloses the Surface Composition of Operating NdBaCo2O5+δ Solid Oxide Fuel Cell Cathodes. *J. Power Sources* **2019**, *436*, 226815.
(40) Gottfried, J. M. Surface Chemistry of Porphyrins and Phthalocyanines. *Surf. Sci. Rep* **2015**, *70*, 259−379.
(41) Auwärter, W.; Écija, D.; Klappenberger, F.; Barth, J. V. Porphyrins at Interfaces. *Nat. Chem.* **2015**, *7*, 105−120.
(42) Corva, M.; Mohamed, F.; Tomsic, E.; Rinaldi, M.; Cepek, C.; Seriani, N.; Peressi, M.; Vesselli, E. Learning from Nature: Charge Transfer and Carbon Dioxide Activation at Single, Biomimetic Fe Sites in Tetrapyrroles on Graphene. *J. Phys. Chem. C* **2019**, *123*, 3916−3922.
(43) Corva, M.; Ferrari, A.; Rinaldi, M.; Feng, Z.; Roiaz, M.; Rameshan, C.; Rupprechter, G.; Costantini, R.; Dell'Angela, M.; Pastore, G.; Comelli, G.; Seriani, N.; Vesselli, E. Vibrational Fingerprint of Localized Excitons in a Two-Dimensional Metal-Organic Crystal. *Nat. Commun.* **2018**, *9*, 4703.
(44) Hattab, H.; N'Diaye, a. T.; Wall, D.; Jnawali, G.; Coraux, J.; Busse, C.; van Gastel, R.; Poelsema, B.; Michely, T.; Meyer zu Heringdorf, F.-J.; Horn-von Hoegen, M. Growth Temperature Dependent Graphene Alignment on Ir(111). *Appl. Phys. Lett.* **2011**, *98*, 141903.
(45) Wurster, B.; Grumelli, D.; Hötger, D.; Gutzler, R.; Kern, K. Driving the Oxygen Evolution Reaction by Nonlinear Cooperativity in Bimetallic Coordination Catalysts. *J. Am. Chem. Soc.* **2016**, *138*, 3623−3626.
(46) Shvets, I. V.; Lübben, O.; Chaika, A. N.; Cafolla, A. A.; Murphy, B. E.; Sergeeva, N. N.; Krasnikov, S. A.; Preobrajenski, A. B.

Homolytic Cleavage of Molecular Oxygen by Manganese Porphyrins Supported on Ag(111). *ACS Nano* **2014**, *8*, 5190−5198.
(47) Tian, C. S.; Shen, Y. R. Recent Progress on Sum-Frequency Spectroscopy. *Surf. Sci. Rep* **2014**, *69*, 105−131.
(48) Shen, Y. R. Surface Properties Probed by Second-Harmonic and Sum-Frequency Generation. *Nature* **1989**, *337*, 519−525.
(49) Corva, M.; Vesselli, E. Room Temperature Carbonylation of Iron−Phthalocyanines Adsorbed on a Single Crystal Metal Surface: An in Situ SFG Investigation at Near-Ambient Pressure. *J. Phys. Chem. C* **2016**, *120*, 22298−22303.
(50) Corva, M.; Feng, Z.; Dri, C.; Salvador, F.; Bertoch, P.; Comelli, G.; Vesselli, E. Carbon Dioxide Reduction on Ir(111): Stable Hydrocarbon Surface Species at near-Ambient Pressure. *Phys. Chem. Chem. Phys.* **2016**, *18*, 6763−6772.
(51) Hayashi, M.; Lin, S. H.; Raschke, M. B.; Shen, Y. R. A Molecular Theory for Doubly Resonant IR−UV-Vis Sum-Frequency Generation. *J. Phys. Chem. A* **2002**, *106*, 2271−2282.
(52) Bonn, M.; Hess, C.; Roeterdink, W. G.; Ueba, H.; Wolf, M. Dephasing of Vibrationally Excited Molecules at Surfaces: CO/Ru(001). *Chem. Phys. Lett.* **2004**, *388*, 269−273.
(53) Zhu, S.; Scardamaglia, M.; Kundsen, J.; Sankari, R.; Tarawneh, H.; Temperton, R.; Pickworth, L.; Cavalca, F.; Wang, C.; Tissot, H.; Weissenrieder, J.; Hagman, B.; Gustafson, J.; Kaya, S.; Lindgren, F.; Källquist, I.; Maibach, J.; Hahlin, M.; Boix, V.; et al. HIPPIE: A New Platform for Ambient-Pressure X-Ray Photoelectron Spectroscopy at the MAX IV Laboratory. *J. Synchrotron Radiat* **2021**, *28*, 624−636.
(54) Bianchi, M.; Cassese, D.; Cavallin, A.; Comin, R.; Orlando, F.; Postregna, L.; Golfetto, E.; Lizzit, S.; Baraldi, A. Surface Core Level Shifts of Clean and Oxygen Covered Ir(111). *New J. Phys.* **2009**, *11*, 063002.
(55) Doniach, S.; Sunjic, M. Many-Electron Singularity in X-Ray Photoemission and X-Ray Line Spectra from Metals. *J. Phys. C Solid State Phys.* **1970**, *3*, 285−291.
(56) Giannozzi, P.; Baroni, S.; Bonini, N.; Calandra, M.; Car, R.; Cavazzoni, C.; Ceresoli, D.; Chiarotti, G. L.; Cococcioni, M.; Dabo, I.; Dal Corso, A.; de Gironcoli, S.; Fabris, S.; Fratesi, G.; Gebauer, R.; Gerstmann, U.; Gougoussis, C.; Kokalj, A.; Lazzeri, M.; et al. QUANTUM ESPRESSO: A Modular and Open-Source Software Project for Quantum Simulations of Materials. *J. Phys.: Condens. Matter* **2009**, *21*, 395502.
(57) Giannozzi, P.; Andreussi, O.; Brumme, T.; Bunau, O.; Buongiorno Nardelli, M.; Calandra, M.; Car, R.; Cavazzoni, C.; Ceresoli, D.; Cococcioni, M.; Colonna, N.; Carnimeo, I.; Dal Corso, A.; de Gironcoli, S.; Delugas, P.; DiStasio, R. A.; Ferretti, A.; Floris, A.; Fratesi, G.; et al. Advanced Capabilities for Materials Modelling with Quantum ESPRESSO. *J. Phys.: Condens. Matter* **2017**, *29*, 465901.
(58) Giannozzi, P.; Baseggio, O.; Bonfà, P.; Brunato, D.; Car, R.; Carnimeo, I.; Cavazzoni, C.; de Gironcoli, S.; Delugas, P.; Ferrari Ruffino, F.; Ferretti, A.; Marzari, N.; Timrov, I.; Urru, A.; Baroni, S. Quantum ESPRESSO toward the Exascale. *J. Chem. Phys.* **2020**, *152*, 154105.
(59) Rappe, A. M.; Rabe, K. M.; Kaxiras, E.; Joannopoulos, J. D. Optimized Pseudopotentials. *Phys. Rev. B* **1990**, *41*, 1227−1230.
(60) Cococcioni, M.; de Gironcoli, S. Linear Response Approach to the Calculation of the Effective Interaction Parameters in the LDA+U Method. *Phys. Rev. B* **2005**, *71*, 035105.
(61) Dias da Silva, L. G. G. V.; Tiago, M. L.; Ulloa, S. E.; Reboredo, F. A.; Dagotto, E. Many-Body Electronic Structure and Kondo Properties of Cobalt-Porphyrin Molecules. *Phys. Rev. B* **2009**, *80*, 155443.
(62) Grimme, S.; Antony, J.; Ehrlich, S.; Krieg, H. A Consistent and Accurate Ab Initio Parametrization of Density Functional Dispersion Correction (DFT-D) for the 94 Elements H-Pu. *J. Chem. Phys.* **2010**, *132*, 154104.
(63) Methfessel, M.; Paxton, A. T. High-Precision Sampling for Brillouin-Zone Integration in Metals. *Phys. Rev. B* **1989**, *40*, 3616−3621.
(64) Pehlke, E.; Scheffler, M. Evidence for Site-Sensitive Screening of Core Holes at the Si and Ge (001) Surface. *Phys. Rev. Lett.* **1993**, *71*, 2338−2341.
(65) Contreras-García, J.; Johnson, E. R.; Keinan, S.; Chaudret, R.; Piquemal, J.-P.; Beratan, D. N.; Yang, W. NCIPLOT: A Program for Plotting Noncovalent Interaction Regions. *J. Chem. Theory Comput* **2011**, *7*, 625−632.
(66) Sit, P. H.-L.; Car, R.; Cohen, M. H.; Selloni, A. Simple, Unambiguous Theoretical Approach to Oxidation State Determination via First-Principles Calculations. *Inorg. Chem.* **2011**, *50*, 10259−10267.
(67) Pletikosić, I.; Kralj, M.; Pervan, P.; Brako, R.; Coraux, J.; N'Diaye, A. T.; Busse, C.; Michely, T. Dirac Cones and Minigaps for Graphene on Ir(111). *Phys. Rev. Lett.* **2009**, *102*, 056808.
(68) Hämäläinen, S. K.; Stepanova, M.; Drost, R.; Liljeroth, P.; Lahtinen, J.; Sainio, J. Self-Assembly of Cobalt-Phthalocyanine Molecules on Epitaxial Graphene on Ir(111). *J. Phys. Chem. C* **2012**, *116*, 20433−20437.
(69) Li, Y.; Xiao, J.; Shubina, T. E.; Chen, M.; Shi, Z.; Schmid, M.; Steinrück, H.-P.; Gottfried, J. M.; Lin, N. Coordination and Metalation Bifunctionality of Cu with 5,10,15,20-Tetra(4-Pyridyl)-Porphyrin: Toward a Mixed-Valence Two-Dimensional Coordination Network. *J. Am. Chem. Soc.* **2012**, *134*, 6401−6408.
(70) Gu, J.-Y.; Cai, Z.-F.; Wang, D.; Wan, L.-J. Single-Molecule Imaging of Iron-Phthalocyanine-Catalyzed Oxygen Reduction Reaction by in Situ Scanning Tunneling Microscopy. *ACS Nano* **2016**, *10*, 8746−8750.
(71) Stein, A.; Rolf, D.; Lotze, C.; Czekelius, C.; Franke, K. J.; Tegeder, P. Electronic Structure of an Iron Porphyrin Derivative on Au(1 1 1). *J. Phys.: Condens. Matter* **2019**, *31*, 044002.
(72) Blom, N.; Odo, J.; Nakamoto, K.; Strommen, D. P. Resonance Raman Studies of Metal Tetrakis(4-N-Methylpyridyl)Porphine: Band Assignments, Structure-Sensitive Bands, and Species Equilibria. *J. Phys. Chem.* **1986**, *90*, 2847−2852.
(73) Araki, K.; Santos, P. S.; de Oliveira, L. F. C. C.; Toma, H. E. Resonance Raman Spectra of a Supramolecular Species Containing Four Ruthenium(II)-Bipyridine Complexes Attached to Zinc-Tetrapyridyl Porphynate. *Spectrosc. Lett.* **1995**, *28*, 119−126.
(74) Kincaid, J. R.; Proniewicz, L. M.; Bajdor, K.; Bruha, A.; Nakamoto, K. Resonance Raman Spectra of Oxyen Adducts of Cobalt Porphyrins. Enhancement of Solvent and Solute Bands via Resonance Vibrational Coupling. *J. Am. Chem. Soc.* **1985**, *107*, 6775−6781.
(75) Streibel, V.; Hävecker, M.; Yi, Y.; Velasco Vélez, J. J.; Skorupska, K.; Stotz, E.; Knop-Gericke, A.; Schlögl, R.; Arrigo, R. In Situ Electrochemical Cells to Study the Oxygen Evolution Reaction by Near Ambient Pressure X-Ray Photoelectron Spectroscopy. *Top. Catal* **2018**, *61*, 2064−2084.
(76) Arrigo, R.; Hävecker, M.; Schuster, M. E.; Ranjan, C.; Stotz, E.; Knop-Gericke, A.; Schlögl, R. In Situ Study of the Gas-Phase Electrolysis of Water on Platinum by NAP-XPS. *Angew. Chemie Int. Ed* **2013**, *52*, 11660−11664.
(77) Favaro, M.; Yang, J.; Nappini, S.; Magnano, E.; Toma, F. M.; Crumlin, E. J.; Yano, J.; Sharp, I. D. Understanding the Oxygen Evolution Reaction Mechanism on CoO x Using Operando Ambient-Pressure X-Ray Photoelectron Spectroscopy. *J. Am. Chem. Soc.* **2017**, *139*, 8960−8970.
(78) Cai, X.; Peng, F.; Luo, X.; Ye, X.; Zhou, J.; Lang, X.; Shi, M. Understanding the Evolution of Cobalt-Based Metal-Organic Frameworks in Electrocatalysis for the Oxygen Evolution Reaction. *ChemSusChem* **2021**, *14*, 3163−3173.
(79) Bai, Y.; Sekita, M.; Schmid, M.; Bischof, T.; Steinrück, H. P.; Gottfried, J. M. Interfacial Coordination Interactions Studied on Cobalt Octaethylporphyrin and Cobalt Tetraphenylporphyrin Monolayers on Au(111). *Phys. Chem. Chem. Phys.* **2010**, *12*, 4336−4344.
(80) Gunnarsson, O.; Schönhammer, K. CO on Cu(100)—Explanation of the Three-Peak Structure in the X-Ray-Photoemission-Spectroscopy Core Spectrum. *Phys. Rev. Lett.* **1978**, *41*, 1608−1612.

https://doi.org/10.1021/acscatal.2c02029
ACS Catal. 2022, 12, 7950−7959

(81) Isvoranu, C.; Wang, B.; Schulte, K.; Ataman, E.; Knudsen, J.; Andersen, J. N.; Bocquet, M. L.; Schnadt, J. Tuning the Spin State of Iron Phthalocyanine by Ligand Adsorption. *J. Phys.: Condens. Matter* **2010**, *22*, 472002.
(82) Biesinger, M. C.; Payne, B. P.; Grosvenor, A. P.; Lau, L. W. M.; Gerson, A. R.; Smart, R. S. C. Resolving Surface Chemical States in XPS Analysis of First Row Transition Metals, Oxides and Hydroxides: Cr, Mn, Fe, Co and Ni. *Appl. Surf. Sci.* **2011**, *257*, 2717−2730.
(83) Goldenstein, C. S.; Miller, V. A.; Mitchell Spearrin, R.; Strand, C. L. SpectraPlot.Com: Integrated Spectroscopic Modeling of Atomic and Molecular Gases. *J. Quant. Spectrosc. Radiat. Transf* **2017**, *200*, 249−257.
(84) Vohringer-Martinez, E.; Hansmann, B.; Hernandez, H.; Francisco, J. S.; Troe, J.; Abel, B. Water Catalysis of a Radical-Molecule Gas-Phase Reaction. *Science* **2007**, *315*, 497−501.
(85) Chuntonov, L.; Kumar, R.; Kuroda, D. G. Non-Linear Infrared Spectroscopy of the Water Bending Mode: Direct Experimental Evidence of Hydration Shell Reorganization? *Phys. Chem. Chem. Phys.* **2014**, *16*, 13172−13181.
(86) Yang, J.; Dettori, R.; Nunes, J. P. F.; List, N. H.; Biasin, E.; Centurion, M.; Chen, Z.; Cordones, A. A.; Deponte, D. P.; Heinz, T. F.; Kozina, M. E.; Ledbetter, K.; Lin, M.-F.; Lindenberg, A. M.; Mo, M.; Nilsson, A.; Shen, X.; Wolf, T. J. A.; Donadio, D.; et al. Direct Observation of Ultrafast Hydrogen Bond Strengthening in Liquid Water. *Nature* **2021**, *596*, 531−535.
(87) Ramasesha, K.; De Marco, L.; Mandal, A.; Tokmakoff, A. Water Vibrations Have Strongly Mixed Intra- and Intermolecular Character. *Nat. Chem.* **2013**, *5*, 935−940.
(88) Singha, A.; Mittra, K.; Dey, A. Effect of Hydrogen Bonding on Innocent and Non-Innocent Axial Ligands Bound to Iron Porphyrins. *Dalt. Trans* **2019**, *48*, 7179−7186.
(89) Petrik, I. D.; Davydov, R.; Ross, M.; Zhao, X.; Hoffman, B.; Lu, Y. Spectroscopic and Crystallographic Evidence for the Role of a Water-Containing H-Bond Network in Oxidase Activity of an Engineered Myoglobin. *J. Am. Chem. Soc.* **2016**, *138*, 1134−1137.
(90) Nagaraju, P.; Ohta, T.; Liu, J.-G.; Ogura, T.; Naruta, Y. The Secondary Coordination Sphere Controlled Reactivity of a Ferric-Superoxo Heme: Unexpected Conversion to a Ferric Hydroperoxo Intermediate by Reaction with a High-Spin Ferrous Heme. *Chem. Commun.* **2016**, *52*, 7213−7216.
(91) Chang, C. J.; Chng, L. L.; Nocera, D. G. Proton-Coupled O−O Activation on a Redox Platform Bearing a Hydrogen-Bonding Scaffold. *J. Am. Chem. Soc.* **2003**, *125*, 1866−1876.

https://doi.org/10.1021/acscatal.2c02029
ACS Catal. 2022, 12, 7950−7959